Energy constraints in forced recirculating MHD flows

By D. KINNEAR[1] and P. A. DAVIDSON[2]

[1]Fluent Europe, Holmwood House, Cortworth Road, Sheffield, S11 9LP, UK

[2]Department of Engineering, Cambridge University, Trumpington Street, Cambridge, CB2 1PZ, UK

We are concerned here with forced steady recirculating flows which are laminar, two-dimensional and have a high Reynolds number. The body force is considered to be prescribed and independent of the flow, a situation which arises frequently in magnetohydrodynamics. Such flows are subject to a strong constraint. Specifically, the body force generates kinetic energy throughout the flow field, yet dissipation is confined to narrow singular regions such as boundary layers. If the flow is to achieve a steady state, then the kinetic energy which is continually generated within the bulk of the flow must find its way to the dissipative regions. Now the distribution of $u^2/2$ is governed by a transport equation, in which the only cross-stream transport of energy is diffusion, $v\nabla^2(u^2/2)$. It follows that there are only two possible candidates for the transport of energy to the dissipative regions: the energy could be diffused to the shear layers, or else it could be convected to the shear layers through entrainment of the streamlines. We investigate both options and show that neither is a likely candidate at high Reynolds number. We then describe numerical experiments for a model problem designed to resolve these issues. We show that, at least for our model problem, no stable steady solution exists at high Reynolds number. Rather, as soon as the Reynolds number exceeds a modest value of around 10, the flow becomes unstable via a supercritical Hopf bifurcation.

1. Introduction: energy constraints in forced, recirculating flows

There are a number of examples of forced recirculating flows where the driving force is prescribed and independent of the motion. Perhaps the most familiar case is the flow of an electrically conducting liquid, say a liquid metal, driven by an oscillating magnetic field. When these flows are steady, laminar and two-dimensional, they must organize themselves to satisfy a particularly strong constraint. That is, each fluid particle which is accelerated by the body force must also pass through a dissipative region of intense shear. If it did not, the energy of the particle would continually increase as it is cycled repeatedly through regions of significant forcing.

Now regions of high shear are, at large Reynolds number, generally confined to narrow, singular regions, such as boundary layers or separated shear layers. How then do such flows arrange for all forced streamlines to be flushed through these narrow sub-domains? This critical yet unresolved question lies at the heart of this paper.

We shall restrict ourselves to the case of an incompressible, two-dimensional, laminar flow driven by a prescribed Lorentz force, F. This force is assumed to originate from a high-frequency magnetic field, and so is confined to a narrow region

(*a*)

Body force
driving the flow

Solid boundary

Secondary eddy   Symmetry line   Primary eddy

(*b*)

Separated   Separation δ_v
shear layer   point

Boundary layer, (region 1)
of thickness δ_v

Boundary layer
(region 1)

Forced region (region 2)
of thickness δ_F

Unforced,
inviscid
region
(region 3)

δ_F

Secondary eddy
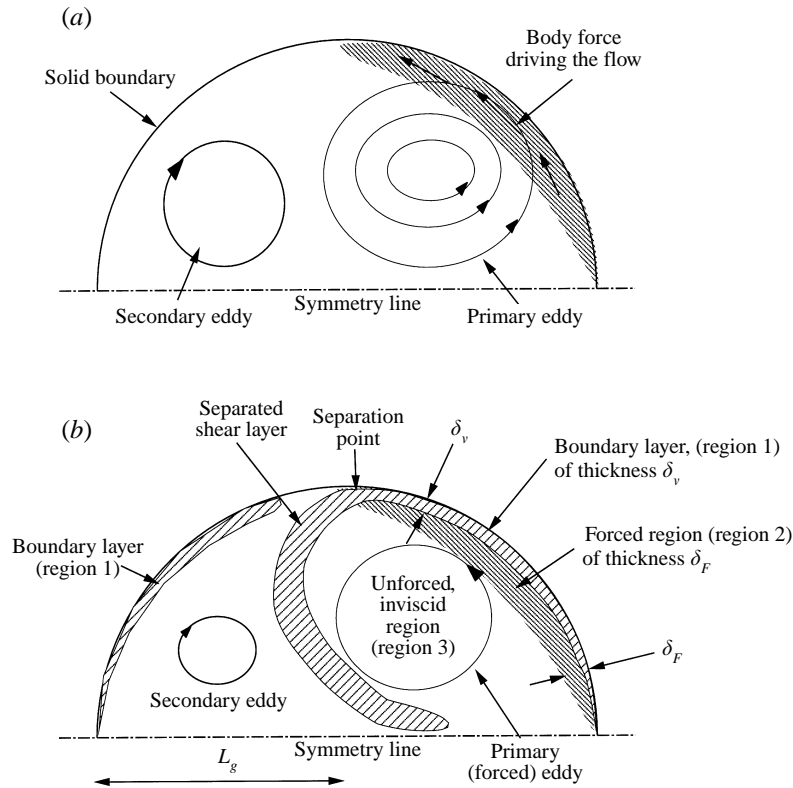
L_g Symmetry line   Primary
(forced) eddy

FIGURE 1. Schematic definition of a forced flow: (*a*) general shape of the flow;
(*b*) possible regions in the flow.

(the skin depth) adjacent to the boundary. The thickness of this region is measured by the skin depth δ_F, defined by

$$\delta_F = \left(\frac{1}{2\mu_0 \sigma \Omega}\right)^{1/2},$$

where Ω is the field frequency, μ_0 is the magnetic permeability and σ is the electrical conductivity.

Throughout this paper we consider the case where the Reynolds number is moderate to large so that, in general, viscous shear stresses can compete with inertia only in narrow, singular regions such as boundary layers. The magnetic Reynolds number, on the other hand, is assumed to be small, so that **F** is independent of the motion, **u**. The situation is as shown schematically in figure 1. Our aim is to establish the structure and scaling of this flow. (We shall discuss shortly the significance of the different regions indicated schematically in figure 1.)

It is convenient to introduce the three length scales: δ_F, δ_v and L_g. As indicated in figure 1, δ_F is the characteristic thickness of the forced region, δ_v is the characteristic thickness of the boundary layer, and L_g is a typical geometric length scale. In most practical situations the skin depth, which is governed by the frequency of the applied magnetic field, and the Reynolds number, which is an inverse measure of viscosity, v, are such that

$$\delta_v \ll \delta_F \ll L_g. \tag{1.1}$$

In laboratory and industrial applications, it is unusual for δ_F to be less than or equal to the boundary layer thickness. Moreover, this ranking of the length scales is the most interesting from a theoretical standpoint. In particular, by specifying $\delta_v \ll \delta_F$, we are forced to address the issue of how energy is transferred from the forced, (almost) inviscid streamlines to the dissipative regions. Consequently, in this paper we focus on flows characterized by (1.1).

In §3 and §4 we shall describe numerical experiments designed to establish the structure of flows with high Reynolds numbers, i.e. $\delta_v \ll \delta_F$. Indeed, there has been a history of papers that discuss this regime (e.g. Fautrelle 1981; Mestel 1984; and Sneyd 1979). However, for reasons which will become evident shortly, we have been unable to achieve a true separation of the three length scales so that our numerical experiments are more accurately characterized by $\delta_v < \delta_F < L_g$. In short, we find that the flow becomes time-dependent at quite moderate Reynolds numbers (around 10).

Another common feature of flows driven by a high-frequency magnetic field is that the forcing is often restricted to only part of the boundary, as indicated in figure 1. Again, we have chosen the distribution of F in our numerical experiments to reflect this. This non-uniformity of the forcing along the boundary is significant to the extent that it tends to promote one or more internal shear layers. We shall postpone a detailed discussion of this point until §3. However, we may give here some indication as to why this should be so. In brief, when the flow adjacent to the boundary leaves the forced region it tends to slow down. This is important because laminar boundary layers are prone to separate whenever the external stream decelerates, giving rise to an internal shear layer and to a relatively weak, secondary eddy. In general, then, we must allow for a multiple eddy structure, comprising primary (forced) vortices, as well as weaker, secondary eddies driven by internal shear.

Our fundamental problem is this. Kinetic energy is generated by F throughout a forced region of thickness δ_F, yet dissipation is generally restricted to thin shear layers which are much narrower than δ_F. If the flow is to achieve a steady state, then there must be some mechanism by which the energy created by F is transported to the dissipative regions. There are two possibilities: either the energy is advected to the shear layers, or else it diffuses across streamlines to the wall (see §2.2). However, neither possibility seems particularly likely. Diffusion of energy requires high transverse gradients in velocity, and these gradients must be large enough to sustain an energy flux equal to the boundary layer dissipation. Yet we have virtually excluded this possibility by insisting that $\delta_v \ll \delta_F$. Transport by advection, on the other hand, seems equally improbable. It relies on some entrainment mechanism by which all forced streamlines are flushed through a boundary layer. While such mechanisms are readily identified in three-dimensional flows, such as Ekman pumping (Davidson 1992; and Davidson, Short & Kinnear 1995), there is no evidence for entrainment in two dimensions. We are left, therefore, with a dilemma.

In order to resolve these issues, we have performed numerical experiments on a model problem. These are described in §3 and §4. However, it is worth stating now our primary conclusion. In brief, the computations suggest that, at least in our model problem, no stable, steady solution exists at high Reynolds numbers. Rather, as soon as the Reynolds number exceeds a modest value, the flow becomes unstable via a supercritical Hopf bifurcation. (This is the point at which δ_v starts to drop significantly below δ_F.)

The plan of this paper is as follows. In §2.1 we review certain previous studies of forced, recirculatory flows. In particular, we focus on the work of Sneyd (1979), Fautrelle (1981) and Mestel (1989). Next, in §2.2 we discuss energy constraints on

forced flows and explain in detail the nature of the dilemma faced by two-dimensional forced flows. In §2.3 and §2.4 we describe possible velocity scalings and flow structures.

In §3 we try to resolve these issues numerically, by performing numerical experiments on a simple model problem. Our main conclusion is that the flow becomes unstable at low values of Reynolds number. Consequently, in §4, we examine the transition to unsteady flow. The discussion in §5 draws together the theoretical and numerical arguments.

2. Previous studies and energy constraints

2.1. *Previous studies*

Broadly speaking, previous studies have been based either on a paper by Batchelor (1956), or else on an integral equation obtained by integrating the Navier–Stokes equations around a closed streamline,

$$\oint_C \boldsymbol{F} \cdot \mathrm{d}\boldsymbol{l} + v \oint_C \nabla^2 \boldsymbol{u} \cdot \mathrm{d}\boldsymbol{l} = 0. \tag{2.1}$$

However, we shall see that, as yet, there is no self-consistent model for the case where $\delta_v \ll \delta_F$. The Prandtl–Batchelor theorem forms the basis of a sequence of papers on this and many other problems. Batchelor was concerned with the general problem of two-dimensional, closed-streamline flows of small viscosity. In particular, he noted that at high Reynolds numbers, those streamlines which avoid both forced and dissipative regions must form eddies of uniform vorticity. The reasoning is straightforward. In the absence of viscous diffusion or forcing, vorticity (ω) is conserved along streamlines $\omega = \omega(\psi)$ (where ψ is the streamfunction). When the viscosity, v, is exactly zero, the variation of ω between streamlines is indeterminate. When v is small but finite, however, cross-stream diffusion eventually eradicates any gradients in vorticity between streamlines, i.e. $\omega'(\psi) = 0$. This is true no matter how small v becomes, provided it remains finite.

This result is particularly powerful for forced flows where there is no separation of the boundary layer, and where the thickness of the forced region is smaller than, or of the order of, the boundary layer thickness. In such cases one simply attributes some unknown, uniform vorticity, ω_0, to the core flow, and then calculates the associated velocity just outside the boundary layer. The boundary layer equations can then be solved (at least in principle) for the wall shear, and the unknown vorticity, ω_0, determined by an integral constraint. This strategy has been adopted by, amongst others, Sneyd (1979) and Fautrelle (1981).

When $\delta_F \gg \delta_v$, however, Batchelor's theorem merely tells us about zones such as region 3 in figure 1. It is not intended to tell us anything about the relationship between the forced and dissipative regions, and in particular, sheds no light on our energy transport dilemma. Moreover, since boundary layer separation is likely to be a common feature of these forced flows, we cannot identify *a priori* the size and shape of the Batchelor regions. Nevertheless, we may expect Batchelor type behaviour to be characteristic of the unforced recirculating regions.

Mestel (1989) has extended Batchelor's theorem, for a restricted class of flows. He considered cases where there is forcing along the streamlines, but where the viscous shear remains small by comparison to inertia. Like Batchelor's theorem, the results apply only to streamlines which avoid all singular, dissipative regions, such as boundary layers. For streamlines which avoid all boundary layers, the integral equation (2.1) suggests that the body force and shear stress gradients are of similar

magnitude and therefore both are small by comparison with inertia. For high Reynolds number, Re, this implies $\omega = \omega(\psi)$, to leading order in Re^{-1}. Now the diffusion of vorticity across a closed streamline is, in the steady state, equal to the source of vorticity within the streamline. Using the expression, $\omega = \omega(\psi)$, in conjunction with the integral equations, we may express this explicitly in the form

$$\frac{\partial \omega}{\partial \psi} = \frac{\oint_C \boldsymbol{F} \cdot \mathrm{d}\boldsymbol{l}}{v \oint_C \boldsymbol{u} \cdot \mathrm{d}\boldsymbol{l}}. \tag{2.2}$$

By implication, $\boldsymbol{u}$ must scale as v^{-1} in such regions.

We might speculate that region 2 in figure 1 is of this form. However, as Mestel (1989) noted, v^{-1} scaling is almost always inappropriate for high-Re flows confined by solid boundaries. It is valid only for cases where the surface shear stress is prescribed (in effect, levitation problems) or else where the inertial forces parallel to the streamlines are very small (circular streamlines). The point is that v^{-1} scaling implies an order of magnitude balance between energy generation and viscous dissipation within the forced region. This is incompatible with the existence of a shear layer whose dissipation exceeds that of the core flow. Of course, v^{-1} scaling also characterizes low-Re flows, but for entirely different reasons.

2.2. *Energy constraints*

We will now quantify the energy arguments above using two-integral equations introduced by, amongst others, Moffatt (1978). Our starting point is the Navier–Stokes equations for steady flow,

$$\frac{\mathrm{D}\boldsymbol{u}}{\mathrm{D}t} = \boldsymbol{u} \cdot \nabla \boldsymbol{u} = -\nabla \left(\frac{p}{\rho} \right) + v \nabla^2 \boldsymbol{u} + \boldsymbol{F},$$

where $\boldsymbol{u}$ is the velocity, p is pressure and ρ is the fluid density. Integrating this around a closed streamline, C, furnishes the well-known energy equation

$$\oint_C \boldsymbol{F} \cdot \mathrm{d}\boldsymbol{l} = -v \oint_C \nabla^2 \boldsymbol{u} \cdot \mathrm{d}\boldsymbol{l} = v \oint_C \left(\frac{\partial u_i}{\partial x_j} \right)^2 \mathrm{d}t - v \oint_C \nabla^2 \left(\frac{\boldsymbol{u}^2}{2} \right) \mathrm{d}t, \tag{2.3}$$

where $\mathrm{d}\boldsymbol{l} = \boldsymbol{u}\mathrm{d}t$ and t is used here in a Lagrangian sense. This represents a balance between the generation, destruction and diffusion of energy. Perhaps the most important characteristic of (2.3) is that *all* forced streamlines must satisfy this constraint; that is, they must all pass through regions of significant shear. We may think of (2.3) as imposing structure on the flow.

A second and closely related (but generally less demanding) energy equation may be obtained from the Navier–Stokes equations. This time we take the product of the momentum equation with $\boldsymbol{u}$ to give

$$\frac{\mathrm{D}}{\mathrm{D}t} \left(\frac{\boldsymbol{u}^2}{2} \right) + \nabla \cdot \left(\frac{p\boldsymbol{u}}{\rho} \right) = \boldsymbol{F} \cdot \boldsymbol{u} + v \nabla^2 \left(\frac{\boldsymbol{u}^2}{2} \right) - v \left(\frac{\partial u_i}{\partial x_j} \right)^2. \tag{2.4}$$

We may interpret this as a transport equation for kinetic energy. The pressure term represents a flux of kinetic energy along a streamline, while the three terms on the right represent the generation, diffusion and destruction of energy. Although the generation of energy, $\boldsymbol{F} \cdot \boldsymbol{u}$ could in principle be positive or negative, our numerical results indicate that its integral ($\int \boldsymbol{F} \cdot \boldsymbol{u} \, \mathrm{d}V$) is always positive.
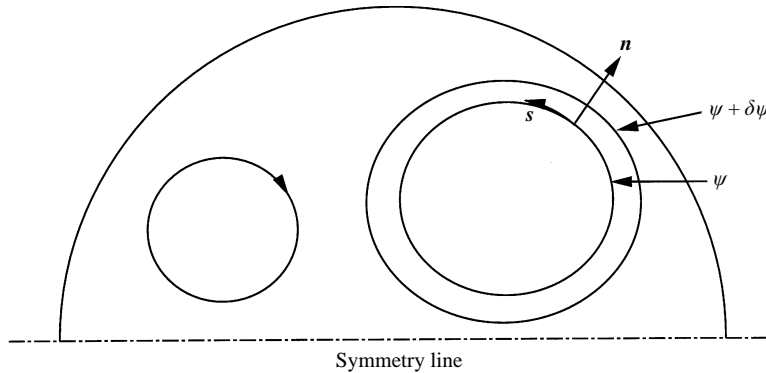
FIGURE 2. Definition of a streamline coordinate system.

Moffatt's second energy equation now arises from integrating (2.4) over the entire flow field. This gives

$$\int_V \boldsymbol{F} \cdot \boldsymbol{u} \, \mathrm{d}V = \nu \int_V \left(\frac{\partial u_i}{\partial x_j} \right)^2 \mathrm{d}V. \tag{2.5}$$

Note that the diffusion term integrates to zero, so that (2.5) represents the global balance between generation and dissipation. Equation (2.5) is attractive because, provided we know the thickness of the dissipative regions, it furnishes a simple estimate for the velocity, u. Indeed, we shall derive this estimate shortly. However, it is essential to note here that any scaling based on (2.5) completely ignores the 'structural' problem of how the energy gets from the forced to the dissipative regions. Evidently, the more demanding, and therefore informative, relationship is the line-integral equation (2.3). It imposes structure on the flow, whereas (2.5) does not.

There is, in fact, a close connection between line integral (2.3) and the global integral (2.5). Equation (2.3) can be obtained from integrating the kinetic energy equation (2.4) over a streamtube, while (2.5) comes, of course, from integrating (2.4) over the entire flow field. To see why this is so, consider the streamtube bounded by streamlines ψ and $\psi + \delta\psi$, where ψ is the streamfunction for $\boldsymbol{u}$ (see figure 2). Integrating (2.4) over the streamtube gives,

$$\oint \boldsymbol{F} \cdot \boldsymbol{u} \, \mathrm{d}V = \nu \oint \left(\frac{\partial u_i}{\partial x_j} \right)^2 \mathrm{d}V - \nu \oint \nabla^2 \left(\frac{\boldsymbol{u}^2}{2} \right) \mathrm{d}V. \tag{2.6}$$

The equivalence of (2.3) and (2.6) is now evident if we note that,

$$\mathrm{d}V = |\mathrm{d}\boldsymbol{l}|\delta n = \frac{-|\mathrm{d}\boldsymbol{l}|\delta\psi}{|\boldsymbol{u}|} = |\delta\psi|\mathrm{d}t.$$

Here δn is the perpendicular distance between the two streamlines. Clearly, we may regard (2.3) as the energy balance for a particular streamtube, whereas (2.5) is obtained by adding all such contributions from individual streamtubes to give the global (or average) energy budget. Because of their similarity, it might be thought that (2.3) and (2.5) should provide identical velocity scales, and indeed this must be the case if the two equations are handled correctly. Interestingly, however, previous authors have obtained quite different scalings for u, depending on which of the integral equations they adopted as their starting point.

2.3. *Contradictory velocity scalings based on different energy integrals*

Previous studies have suggested a variety of scalings for u, including v^{-1}, $v^{-1/3}$, and v^0. To place the rest of this paper in context, it is useful to identify now how these scalings for u arise. (We do not claim at this point that these scalings are actually valid in forced recirculating flows. Indeed, we shall show that some of these scalings are mutually contradictory.) First however, it is necessary to introduce two forms of Reynolds number. We start by noting that the ratio of inertial to viscous forces in the forced region is

$$\frac{\text{Inertia}}{\text{Shear}} \sim \frac{u\delta_F^2}{vL_g},$$

and so it is natural to define Re as

$$Re = \frac{u\delta_F^2}{vL_g}.$$

Here, u might be taken as the maximum velocity in the flow field. However, we do not have an imposed velocity scale, and so it is useful to introduce a second Reynolds number, R_F, based on an artificial velocity scale constructed from the forcing: $(FL_g)^{1/2}$. This second Reynolds number is

$$R_F = \frac{u^*\delta_F^2}{vL_g}; \quad u^* = (FL_g)^{1/2}.$$

It turns out that, in most of our numerical experiments, u and u^* are of similar magnitude, so that often (but not always) R_F may be interpreted as the true Reynolds number, Re.

We shall now estimate u using the two energy integrals. Our starting point is to determine δ_v. In fact, it is not difficult to show that

$$\delta_v \sim \left(\frac{vL_u}{u}\right)^{1/2}, \tag{2.7}$$

where L_u is the characteristic length scale for streamwise gradients in $|\boldsymbol{u}|$ outside the boundary layer. Often, but not always, L_u will equal the geometric length scale, L_g. For an inertial flywheel (i.e. a flow with near circular streamlines), on the other hand, L_u greatly exceeds L_g. We may establish (2.7) as follows. Let U be the velocity immediately outside the boundary layer. In local wall coordinates, s and n, the boundary layer equation is then

$$\boldsymbol{u}\cdot\nabla u_s - v\frac{\partial^2 u_s}{\partial n^2} = -\frac{\mathrm{d}}{\mathrm{d}s}\left(\frac{p}{\rho}\right) + F_s(s) = U\frac{\mathrm{d}U}{\mathrm{d}s}.$$

Here the variation of $\boldsymbol{F}$ across the boundary layer has been ignored, since $\delta_F \gg \delta_v$. Given that the velocity falls to zero at the wall, this tells us that

$$\frac{v}{\delta_v^2} \sim \frac{\mathrm{d}U}{\mathrm{d}s}.$$

Expression (2.7) then follows. Note that the ratio of δ_F to δ_v is given by

$$\left(\frac{\delta_F}{\delta_v}\right)^2 \sim \left(\frac{L_g}{L_u}\right)Re,$$

so that, when $L_u \sim L_g$, a high value of Re ensures that the boundary layer thickness

is much less than δ_F. We shall see that a high value of R_F is also sufficient to ensure $\delta_v \ll \delta_F$.

Having established δ_v, we may use the global (or averaged) energy equation (2.5) to estimate u. If we assume that there is a single velocity scale, u_g, throughout the flow field, then

$$\frac{u_g}{u^*} \sim R_F^{1/3} \left(\frac{L_u}{L_g} \right)^{1/3} \qquad \text{(Global balance)}. \qquad (2.8)$$

Here the subscript 'g' (for global) is to distinguish this estimate of u from those which follow. When L_u is set equal to L_g, we obtain,

$$u_g \sim u^* R_F^{1/3}$$

which has been established by several authors, most notably Mestel (1984). Note that we have failed to resolve the issue of how energy is transported from the forced to the dissipative regions, so we must regard (2.8) with some caution. Indeed, using the same estimate of δ_v with line integral (2.3) furnishes some apparently different and contradictory scalings. If we take a streamline which passes through the boundary layer (region 1 in figure 1), then (2.3) and (2.7) require

$$\frac{u_1}{u_*} \sim \left(\frac{L_u}{L_v} \right)^{1/2} \qquad \text{(Region 1)} \qquad (2.9)$$

where L_v is yet another length scale: the length of the streamline in the shear layer. (Typically, L_v will be equal to L_g, but this need not be the case.) On the other hand, for a forced streamline which manages to avoid all the shear layers (region 2 of figure 1), equation (2.3) demands

$$\frac{u_2}{u_*} \sim R_F \qquad \text{(Region 2)}. \qquad (2.10)$$

Scaling (2.10) is that described by Mestel (1989). Now if we accept that L_u and L_v are both of order L_g, a point to which we return later, then we appear to have three incompatible scalings for u: v^{-1} (from (2.10)), $v^{-1/3}$ (from (2.8)) and v^0 (from (2.9)). Certainly (2.9) and (2.10) seem contradictory, since we would expect the velocity scale in region 2 to dictate the boundary layer velocity. Moreover, both (2.9) and (2.10) appear to contradict estimate (2.8) which is based on the global (or averaged) equation. Expression (2.9) (apparently) gives a lower velocity than (2.8), reflecting the fact that streamlines passing through the boundary layer receive more dissipation than average, while estimate (2.10) gives a velocity higher than (2.8), presumably because streamlines which avoid the boundary layer receive less dissipation than average.

Of course, the reason for these apparent discrepancies is that we have failed to identify a flow structure which allows all of the forced streamlines to dump their excess energy. Until such a structure is identified, any estimate based on the integral equations is difficult to defend and quite likely to be incorrect.

2.4. *Possible flow structures*

We now discuss possible flow structures for forced, laminar, high-Reynolds-number flows in closed, two-dimensional domains. Possible components of such a flow include a constant vorticity (Batchelor) core, a forced boundary layer, and a circular streamline (inertial flywheel) flow.

At higher Reynolds numbers the energy imparted to fluid particles in the forced region must be transported to regions of significant shear where it is dissipated.

Previous papers which have presented numerical results for this regime (Fautrelle 1981 and Mestel 1984) are limited to Reynolds numbers similar to those at which we find an unsteady flow. The definition of Reynolds number used in §2.3 has been specifically chosen to reflect the ratio of inertia to viscous forces in the forced region and differs from those used by Fautrelle (1981) and Mestel (1984). To make a sensible comparison we therefore converted the Reynolds number quoted in their papers to the R_F defined here. Our work indicates the onset of an unsteady flow at about $R_F = 10$ whereas Fautrelle and Mestel seem to achieve steady flows for R_F upto about 50. However, Fautrelle indicates that numerical diffusion will affect his results at the higher Reynolds numbers. The structure of these flows was considered to be a constant vorticity core flow matched to a high shear forced boundary layer. Crucially, however, the issue of how the energy gets from the forced region to the thin boundary layers is not addressed in these papers. It cannot be cross-stream diffusion, since, for $\delta_F \gg \delta_v$, the transverse gradient in velocity is insufficient to support a large enough energy flux across the forced region. Nor is it likely to be advection, since there is no entrainment of the streamlines into the boundary layers. Interestingly, we find in our model problem that the flow goes unstable whenever R_F is high enough to begin to separate δ_F and δ_v.

Another possible feature of flows with $\delta_F > \delta_v$ is the circular (flywheel) type flow observed by Clever & Busse (1981). It is first necessary to note that for low Prandtl numbers flows (with Prandtl number < 1), the buoyancy forces penetrate the core flow within the viscous boundary layers. Such flows might be expected to display similar features to magnetically driven flows with $\delta_F > \delta_v$. Clever & Busse (1981) investigated low-Prandtl-number buoyancy-driven flow between a hot base and a cold top. This consists of a pair of convection rolls which transfer heat between the plates. Their numerical results show that as the Prandtl number decreases (i.e. as the body forces penetrate further into the core flow), the convection rolls become more circular despite the rectangular geometry. As we will see, the main recirculating eddy in our numerical results displays a tendency to become circular as R_F is increased but before the flow goes unsteady.

3. Numerical experiments I: steady flows

3.1. *Definition of a model problem*

To study the structure and scaling of the forced flow shown schematically in figure 1 we have chosen a specific geometry and force distribution.

The model problem consists of a two-dimensional circular domain of radius R with a body force tangential to the boundary and symmetric about $\theta = 0$. This is shown in figure 3 where the (r, θ) coordinate system is defined. The force in the θ-direction, F_θ, decays exponentially with distance from the surface (with length scale δ_F) and is defined by

$$F_\theta = F_0 \sin(2\theta) \exp\left(-(R-r)/\delta_F\right) \qquad \text{on} \qquad 0 \leqslant \theta \leqslant \tfrac{1}{2}\pi,$$
$$F_\theta = 0 \qquad \text{on} \qquad \tfrac{1}{2}\pi < \theta \leqslant \pi.$$

Here we have arbitrarily chosen a force distribution which only acts over half the flow domain. This is typical of many real problems, for example, in cold crucibles, electromagnetic casters or induction furnaces where the rotational force is significant only near restricted parts of the surface. In the computations there are two parameters
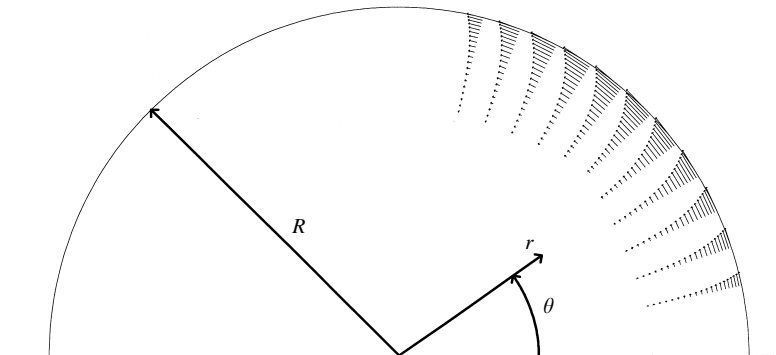
FIGURE 3. Definition of a model forced flow problem.

which we vary. One is the Reynolds number,

$$R_F = \frac{u^* \delta_F^2}{v R}; \quad u^* = (F_0 R)^{1/2},$$

and the other is the forced-region transverse length scale, expressed in a dimensionless form,

$$\epsilon = \frac{\delta_F}{R}.$$

It is also useful to introduce two properties of the flow which enable us to characterize the evolution of a particular flow from an initial condition of $u = 0$ at $t = 0$ to its final state at large t. The first is the maximum velocity u_{max} which is made dimensionless using the velocity scale, u^*. The second is the global kinetic energy of the fluid, E_k,

$$E_k = \frac{1}{(u^*)^2 R^2} \int_V \frac{u^2}{2} \, \mathrm{d}V.$$

This has also been made dimensionless.

We will see that above a critical Reynolds number the flow becomes unsteady and oscillates about a mean structure. In this case we calculate a time-averaged velocity, $\overline{u_{max}}/u^*$ and kinetic energy $\overline{E_k}$, by integrating over a time scale much longer than the period of oscillation.

Figure 7 below shows the streamlines of a typical solution. The flow consists of a primary eddy driven by the forcing and a weaker secondary eddy driven by shear.

3.2. Numerical methods

The momentum and continuity equations were solved for the velocity and pressure distributions using a finite element method and bi-linear quadrilateral elements. A discretization based on the Galerkin method was used to derive matrix equations which furnish the velocities at the nodes and the pressure in each element. Evolution of the flow from rest at $t = 0$ was calculated using Crank–Nicolson time stepping. More details of the numerical method and its application to the time-dependent flow over a step can be found in Pain (1991).

In any numerical experiment it is essential to ensure adequate resolution in time and space. The finite element grid shown in figure 4 was constructed from two blocks so that a good resolution of the boundary layer was possible. To test the resolution in our computations we used several successively smaller time steps and three different
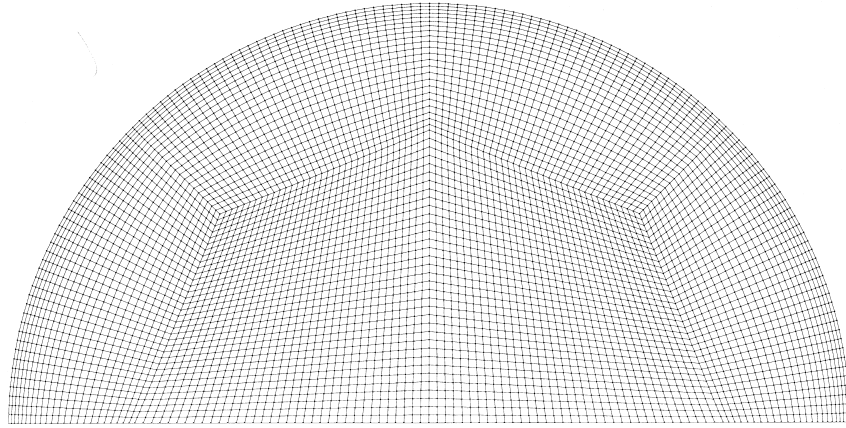
FIGURE 4. Finite element grid with 5799 nodes used for numerical simulation of the model problem.

R_F	Grid	u_{max}/u^*	E_k	E_v	E_F
Steady 8	1458 nodes	1.525	0.4614	0.07220	0.07224
	3216 nodes	1.534	0.4658	0.07310	0.07307
	5799 nodes	1.532	0.4667	0.07304	0.07305
Unsteady 11.5		$\bar{u}_{max}/(F_0 R)^{1/2}$	$\bar{E}_k$	$\bar{E}_v$	$\bar{E}_F$
	1458 nodes	1.982	0.6802	0.08631	0.08659
	3216 nodes	1.968	0.6681	0.08649	0.08679
	5799 nodes	1.969	0.6720	0.08649	0.08694

TABLE 1. Maximum velocity and integrated flow properties for the two simulations and three different grid resolutions with $\epsilon = 0.1$.

grids. Further, we tested the global energy balance by evaluating and comparing the global energy production rate and the global dissipation. In a dimensionless form these are

$$E_F = \frac{1}{F_0^{3/2} R^{5/2}} \int_V \boldsymbol{F} \cdot \boldsymbol{u} \, dV \quad \text{and} \quad E_v = \frac{1}{F_0^{3/2} R^{5/2}} \int_V 2v S_{ij}^2 \, dV,$$

where S_{ij} is the strain rate. Table 1 shows u_{max}/u^*, E_k, E_F and E_v at $R_F = 8$ and their time-averaged counterparts for an unsteady flow at $R_F = 11.5$, both with $\epsilon = 0.1$. Improving the grid resolution improves the global energy balance but only by a relatively small amount. The 5799 node grid was used in all the calculations described below.

The time step was chosen so that the Courant number, $\sigma_c = U \Delta T / \Delta x$, was less than 1 (where U, ΔT and Δx are the characteristic velocity, time-step and element size). Smaller time steps were used to simulate the unsteady flow with typical Courant numbers of order 0.15.

3.3. Numerical solutions

The numerical solutions of the model problem were performed to resolve the issue of how the energy is transported from forced, 'almost' inviscid streamlines to the dissipative regions.
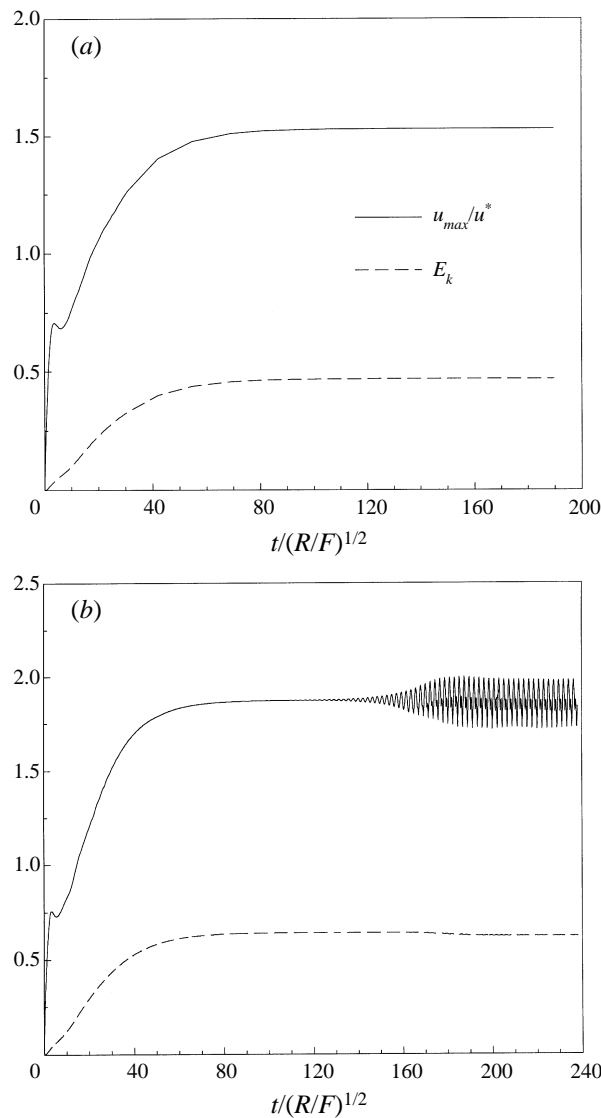
FIGURE 5. Evolution of the maximum velocity and integrated quantities, with $\epsilon = 0.1$ and
(a) $R_F = 8$, (b) $R_F = 10.5$.

Our first observation was that, as the Reynolds number was increased, the flow became unsteady. This is illustrated in figure 5 which shows evolution of u_{max}/u^* and E_k from $t = 0$ to a steady flow at $R_F = 8$, or to an oscillating, steady-on-average flow at $R_F = 10.5$. At the lower Reynolds number, the curves become horizontal as the steady solution is approached. At $R_F = 10.5$, the curves again approach the horizontal, but oscillations develop.

Figure 6 shows the scaling of maximum velocity with Reynolds number at four different values of ϵ. At high Reynolds numbers the flow was unsteady and so a time-averaged maximum velocity of the steady-on-average flow was used. At low Reynolds numbers (approximately $R_F < 10$), the velocity scaling is

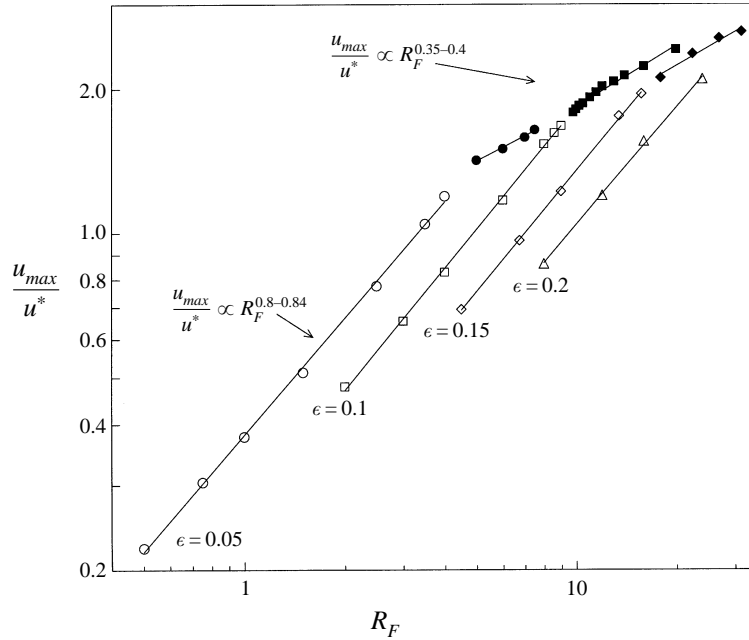$$\frac{u_{max}}{u^*} \sim R_F^n, \quad n = 0.8\text{--}0.84.$$

FIGURE 6. Scaling of dimensionless velocity u_{max}/u^* with R_F. Filled symbols represent time-averaged results for unsteady flows.

This is probably associated with low-Reynolds-number scaling or else the formation of an inertial flywheel ($n = 1$). At higher Reynolds numbers (approximately $R_F > 10$), the scaling of the unsteady flows is

$$\frac{\bar{u}_{max}}{u^*} \sim R_F^n, \quad n = 0.35\text{--}0.4.$$

The figure shows a marked transition between scalings at the critical Reynolds number, and also that the critical Reynolds number is higher at higher values of ϵ.

In the next section we return to examine these unsteady flows. Here we focus on the steady flows just below the critical Reynolds number.

Figure 7 shows the streamlines for three cases with $\epsilon = 0.05$, $\epsilon = 0.1$ and $\epsilon = 0.2$. These are steady flows just below the critical Reynolds number and have $R_F = 4.5$, 8.0 and 24 respectively. The flow consists of a primary eddy driven by the forcing and a weaker shear-driven secondary eddy. The boundary layer has separated resulting in an internal shear layer.

The differences between these cases are difficult to see on the streamline plots. However, contours of constant vorticity shown in figure 8 give a better idea of structure. They illustrate an apparent invariance of vorticity along streamlines in the primary eddy ($\omega = \omega(\psi)$). For the case where ϵ is small ($\epsilon = 0.05$), there is only a small variation in vorticity across the primary eddy. At larger values of ϵ, there is a significant variation in vorticity across the primary eddy. This could constitute a region governed by (2.2), although the Reynolds number is not large enough to strictly justify this. Alternatively, this could indicate the formation of an inertial flywheel, which also satisfies $\omega = \omega(\psi)$.

At first glance figure 8 appears to indicate a clear boundary layer structure, indicative of a high value of Re. However, this is misleading. It should be remembered
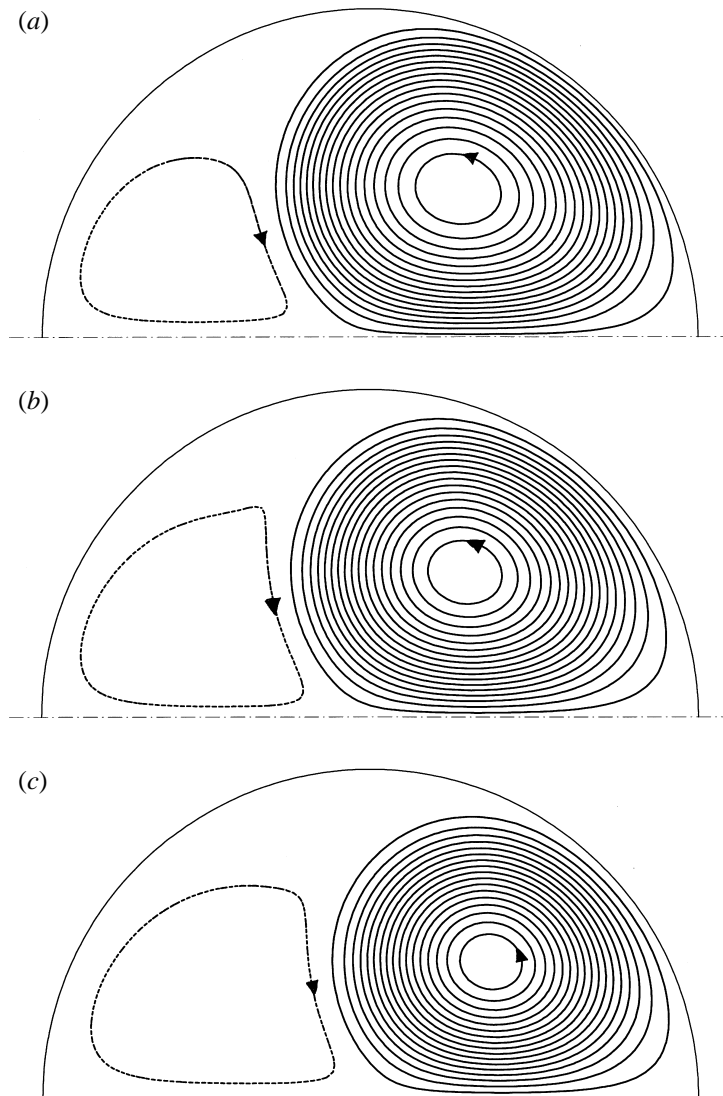
FIGURE 7. Streamlines for steady solutions of the model problem. (*a*) $\epsilon = 0.05$, $R_F = 4.5$; (*b*) $\epsilon = 0.1$, $R_F = 8.0$; (*c*) $\epsilon = 0.2$, $R_F = 24$. Negative contours are dashed.

that the forcing is concentrated in a relatively narrow region, of thickness δ_F, and so we would expect to see vorticity gradients concentrated near the boundary, whether or not boundary layers form. To determine whether we have a high-*Re* boundary-layer structure, we must look at the relative sizes of δ_v and δ_F. The size of δ_v may be estimated from the vorticity contour separating regions of positive and negative vorticity. The size of δ_F may be estimated from the innermost vorticity contour. Evidently, for cases $R_F = 4.5$ and $R_F = 8.0$ there is no significant difference in δ_v and δ_F. It is only in the case $R_F = 24$ that we begin to see some separation of these length scales.

Despite the relatively low Reynolds number of all these steady flows the dissipation is concentrated near the boundary and in the shear layers. This is shown in figure 9 where contours of constant dissipation function have been plotted for the three
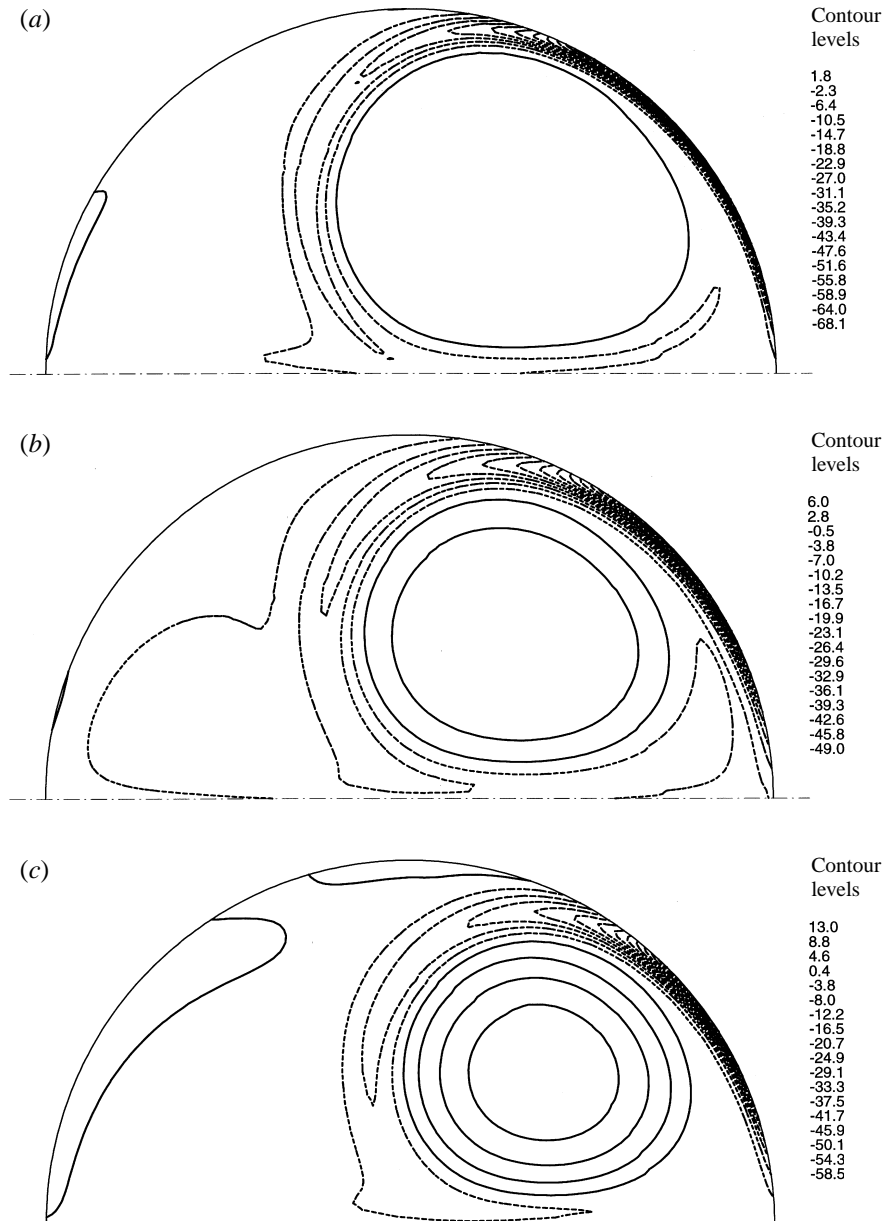
(a)

Contour
levels

1.8
-2.3
-6.4
-10.5
-14.7
-18.8
-22.9
-27.0
-31.1
-35.2
-39.3
-43.4
-47.6
-51.6
-55.8
-58.9
-64.0
-68.1

(b)

Contour
levels

6.0
2.8
-0.5
-3.8
-7.0
-10.2
-13.5
-16.7
-19.9
-23.1
-26.4
-29.6
-32.9
-36.1
-39.3
-42.6
-45.8
-49.0

(c)

Contour
levels

13.0
8.8
4.6
0.4
-3.8
-8.0
-12.2
-16.5
-20.7
-24.9
-29.1
-33.3
-37.5
-41.7
-45.9
-50.1
-54.3
-58.5

FIGURE 8. Contours of constant vorticity ω_z (s^{-1}) for steady solutions of the model problem. (a) $\epsilon = 0.05$, $R_F = 4.5$; (b) $\epsilon = 0.1$, $R_F = 8.0$; (c) $\epsilon = 0.2$, $R_F = 24$. Negative contours are dashed.

cases. Again, the apparent concentration of dissipation near the boundary is more a reflection of the narrowness of the forcing region than of high-Re behaviour.

To investigate how individual fluid particles gain and lose their energy we have traced fluid particles along three different streamlines for a case with $\epsilon = 0.1$, $R_F = 8$. In figure 10 we show these fluid paths together with profiles of particle vorticity (ω) forcing ($\boldsymbol{F} \cdot \hat{\boldsymbol{e}}_s$) and shear stress ($\nu\nabla^2\boldsymbol{u} \cdot \hat{\boldsymbol{e}}_s$) acting on the fluid particle as it passes around the streamline. (Here, $\hat{\boldsymbol{e}}_s$ is a unit vector along the streamline and the origin of the streamline coordinates for each streamline is shown in the figure.) The first
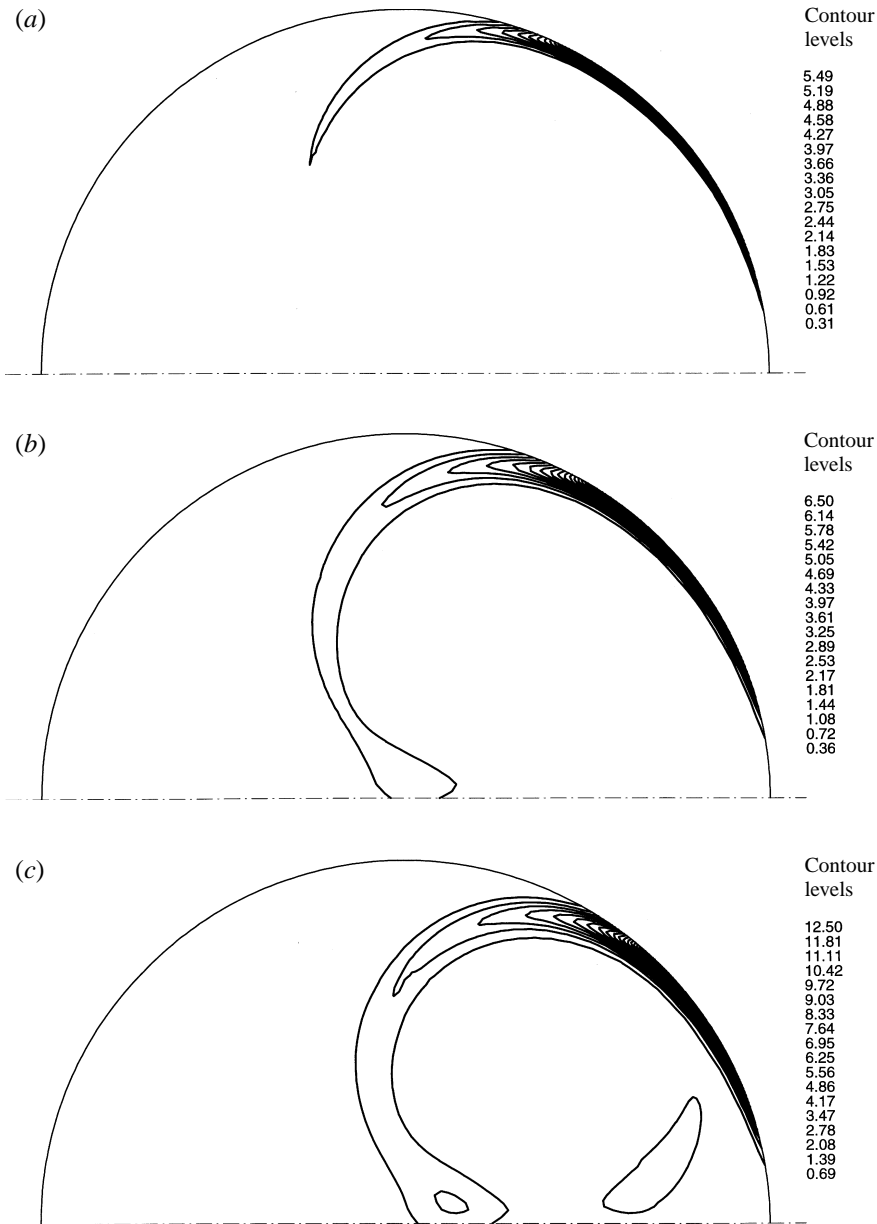
(*a*)

Contour
levels

5.49
5.19
4.88
4.58
4.27
3.97
3.66
3.36
3.05
2.75
2.44
2.14
1.83
1.53
1.22
0.92
0.61
0.31

(*b*)

Contour
levels

6.50
6.14
5.78
5.42
5.05
4.69
4.33
3.97
3.61
3.25
2.89
2.53
2.17
1.81
1.44
1.08
0.72
0.36

(*c*)

Contour
levels

12.50
11.81
11.11
10.42
9.72
9.03
8.33
7.64
6.95
6.25
5.56
4.86
4.17
3.47
2.78
2.08
1.39
0.69

FIGURE 9. Contours of constant dissipation function Φ for steady solutions of the model problem.
(*a*) $\epsilon = 0.05$, $R_F = 4.5$; (*b*) $\epsilon = 0.1$, $R_F = 8.0$; (*c*) $\epsilon = 0.2$, $R_F = 24$.

point to note is that contributions to $\oint \nu \nabla^2 \boldsymbol{u} \cdot \mathrm{d}\boldsymbol{l}$ and $\oint \boldsymbol{F} \cdot \mathrm{d}\boldsymbol{l}$ are essentially constant signed. We now consider each streamline in turn.

Streamline (i): In the core of the primary eddy, the vorticity and shear stresses are relatively constant along the streamline.

Streamline (ii): The force acting on the fluid particle as it enters the forced region increases its vorticity. Further along the path the fluid particle enters a region of significant shear stress which results in a fall in vorticity. The shear stress is associated
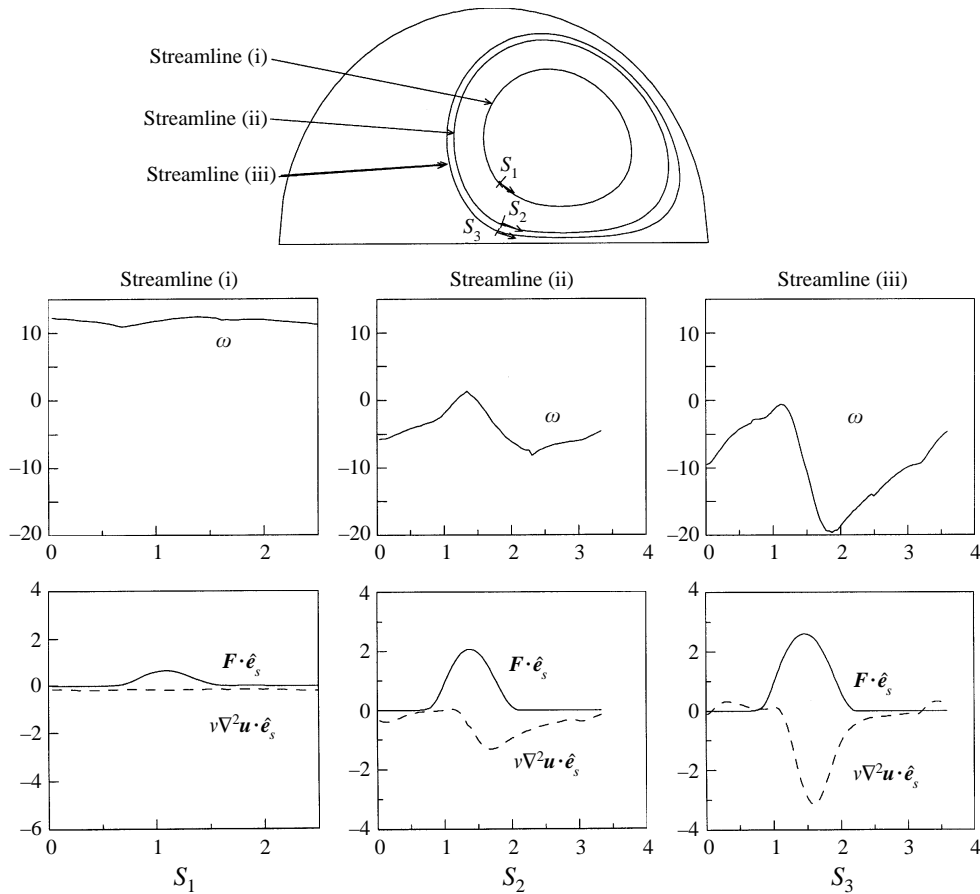
FIGURE 10. Profiles of ω_z (vorticity), $\boldsymbol{F} \cdot \hat{\boldsymbol{e}}_s$ and $\nu\nabla^2\boldsymbol{u} \cdot \hat{\boldsymbol{e}}_s$ for $\epsilon = 0.1$, $R_F = 8$ along three streamlines.

with the boundary layer and separated shear layer. (We use the term boundary layer rather loosely here, since there is no real high-Re structure.)

Streamline (iii): This passes close to the boundary. The forcing and shear stress terms are of equal magnitude and almost coincide. This is associated with the streamline passing into the 'boundary layer' within the forced region.

In summary, the steady flows are observed to scale with $R_F^{0.8-0.84}$. At first glance the innermost streamlines show some features expected of high Reynolds number flow, particularly $\omega = \omega(\psi)$. However, this could equally well be explained by the formation of an inertial flywheel. Certainly, we obtain no clear separation of δ_ν and δ_F which would indicate a high-Re structure. Truly high-Reynolds-number steady flows are never obtained as the flow becomes unsteady when a critical Reynolds number of around 10 is achieved. For streamlines close to the boundary the work done by the body forces on fluid particles is dissipated in the boundary layer and shear layer. For streamlines in the core of the primary eddy, relatively uniform weak shear acts all the way along the streamlines.

Perhaps the most striking feature of the numerical experiments is the sudden change in scaling ($R_F^{0.8}$ to $R_F^{0.35}$) associated with the transition to unsteady flow. We now examine this transition in more detail.
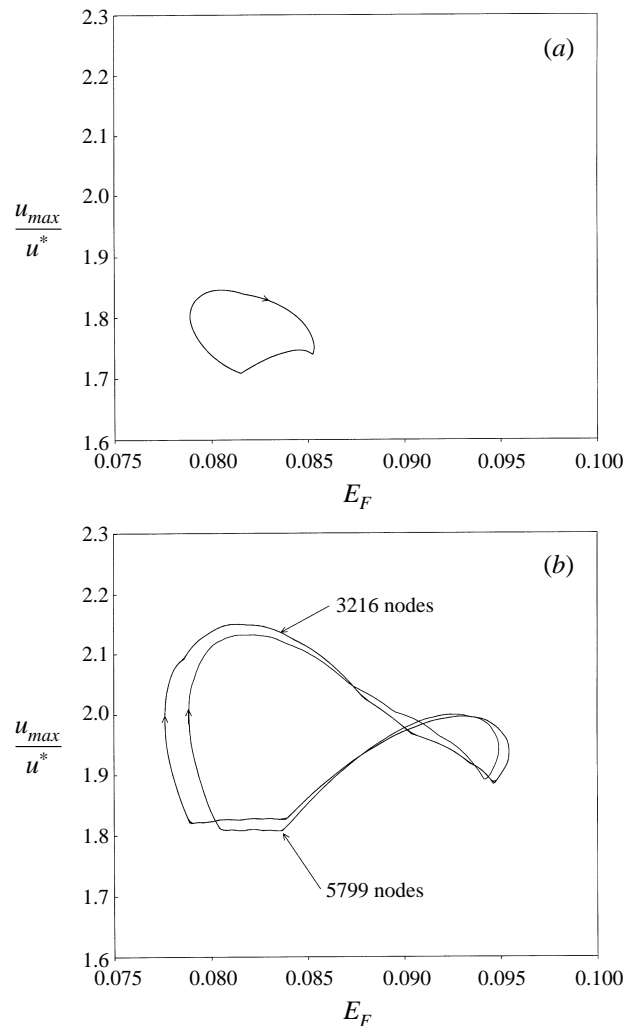
FIGURE 11. Phase diagrams for the unsteady flow with $\epsilon = 0.1$. Maximum velocity is plotted against energy generation rate, E_F. (a) $R_F = 9.8$; (b) $R_F = 11.5$.

4. Numerical experiments II: unsteady flows

In the previous section we found that as the Reynolds number was increased the flow became unsteady. In this section we will see that the unsteady flow just above the critical Reynolds number is due to the periodic shedding of blobs of vorticity from the separation point in the boundary layer.

4.1. *Numerical solutions of unsteady flows*

In our numerical studies we solved the time-dependent Navier–Stokes equations and observed the evolution of the flow with time. At low Reynolds numbers the solution converges to a steady solution. However, if the steady flow is unstable then any perturbation in the initial transient (perhaps due to truncation error) can grow, leading to oscillations in the final flow. The final solutions we obtained consisted of a mean (steady-on-average) flow plus a finite-amplitude oscillation.

The periodicity of the steady-on-average solutions is best illustrated using phase diagrams such as those shown in figure 11. Here we have shown maximum velocity u_{max}/u^* plotted against E_F for $R_F = 9.8$ and $R_F = 11.5$ with $\epsilon = 0.1$. In both cases we found closed limit cycles with a period of about 2 dimensionless time units $(t/(R/F_0)^{1/2})$.

It is, of course, possible that inadequate resolution may lead to numerical oscillations. In our solutions we used two different grids and found that the phase diagrams for each had a very similar limit cycles (see figure 11*b*). We gradually reduced the time step size until we were sure that it did not influence the time history. Finally, we used different initial conditions and checked that the same steady-on-average solutions were obtained. We are confident therefore that our unsteady solutions are genuine.

A sequence of constant vorticity contours covering one limit cycle of an unsteady flow with $\epsilon = 0.1$ and $R_F = 11.5$ are shown in figure 12. As for steady flows, negative vorticity is convected from the boundary layer separation point into the interior region. As this approaches the symmetry boundary it spreads and eventually a blob of negative vorticity breaks away. This blob is convected into the secondary eddy where it retains its form until it is diffused or dissipated.

When the Reynolds number was increased from 11.5 to 13.0 a more complex behaviour was observed. This is illustrated in figure 13. Here, two oscillation frequencies are now evident, one associated with the shedding of blobs of vorticity from the boundary layer, and a much longer one associated with a time scale twelve times the first. The phase diagram for $R_F = 13.0$ is not closed. An examination of the vorticity contours (figure 14) indicates that the vortex blobs shed from the boundary are now more intense and interact with the primary eddy. However, we have been unable to identify the origin of the new, longer time scale.

When the Reynolds number is increased yet further, the flow becomes even more complicated losing all periodicity. No closed limit cycles were obtained at values of R_F greater than about 13.

This unsteady flow can be characterized by a transition from a steady, stable flow to an unsteady but periodic flow. In nonlinear stability theory, such a transition is characteristic of a supercritical Hopf bifurcation. Further, Landau's equation (see for example Drazin & Reid 1991) predicts that just above the critical Reynolds number, $(R_F)_c$,

$$|A| \propto (R_F - (R_F)_c)^{1/2}, \tag{4.1}$$

where $|A|$ is the amplitude of oscillation.

We have investigated the flow just above the critical Reynolds number to obtain the bifurcation diagrams at two values of ϵ. In figure 15 we have plotted the amplitude of oscillation of the maximum velocity against Reynolds number. Curves in the form of (4.1) have been fitted to those results just above the critical Reynolds number. Close to the critical Reynolds number, (4.1) provides a reasonable model for the amplitude; however at higher R_F, the amplitude lies below the curve.

The critical Reynolds numbers for four different values of ϵ are shown in table 2. For $\epsilon = 0.1$ and $\epsilon = 0.15$ the critical Reynolds number is estimated from the curves fitted to the oscillation amplitude data (see figure 15). For $\epsilon = 0.05$ and $\epsilon = 0.2$ the range given in table 2 represents the nearest computed steady and unsteady flow respectively. Very roughly, the critical value of R_F is given by $(R_F)_c \sim 100\epsilon$, so that the transition to periodic flow occurs at $u^*\delta_F/v \sim 100$.

In summary, above the critical Reynolds number the flow becomes unsteady and periodic. In keeping with predictions of Landau's equation, the amplitude of

$t = 0.2$

$t = 1.2$

$t = 0.4$

$t = 1.4$

$t = 0.6$

$t = 1.6$
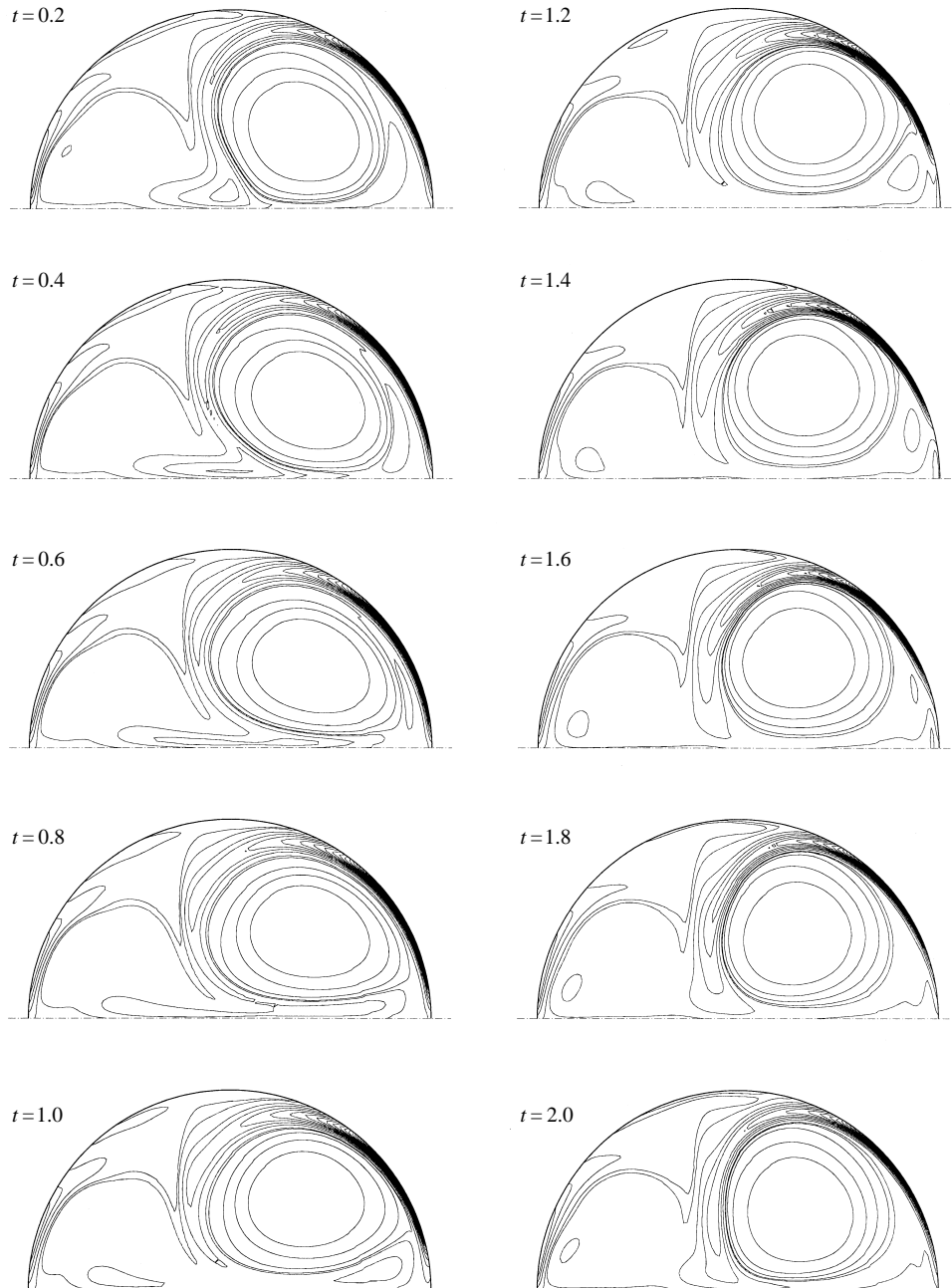
$t = 0.8$

$t = 1.8$

$t = 1.0$

$t = 2.0$

FIGURE 12. A sequence of instantaneous constant vorticity contour plots for one limit cycle with $\epsilon = 0.1$, $R_F = 11.5$.

oscillation increases as the Reynolds number increases above the critical value. At each value of ϵ, the critical Reynolds number is fairly low ($(R_F)_c < 26$). We have not been able to obtain a steady solution at a truly high Reynolds number in our computations.
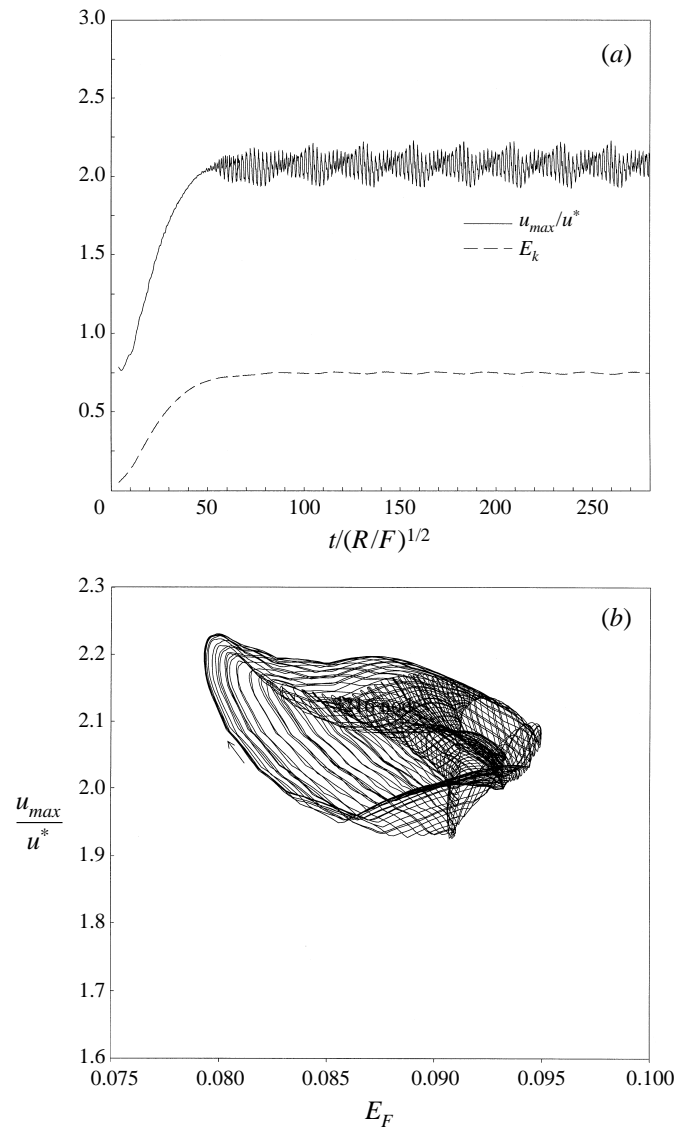
FIGURE 13. (*a*) Evolution of u_{max}/u^* and E_k and (*b*) phase diagram for the unsteady flow, for $R_F = 13$, $\epsilon = 0.1$.

5. Discussion

In §1 we outlined a long-standing dilemma associated with forced, laminar, high-Reynolds-number flows in closed two-dimensional domains. In brief, mechanical energy is generated throughout the flow, yet dissipation is confined to narrow subdomains. If the flow is to achieve a steady state then energy must be transferred from one region to the other, yet there seems to be no obvious mechanism for this. Specifically, transport by advection seems unlikely because, in two dimensions, no entrainment mechanism has yet been identified which categorically ensures that all forced streamlines pass through a boundary layer. Transport of energy by diffusion, on the other hand, seems equally unlikely, as this requires internal velocity gradients
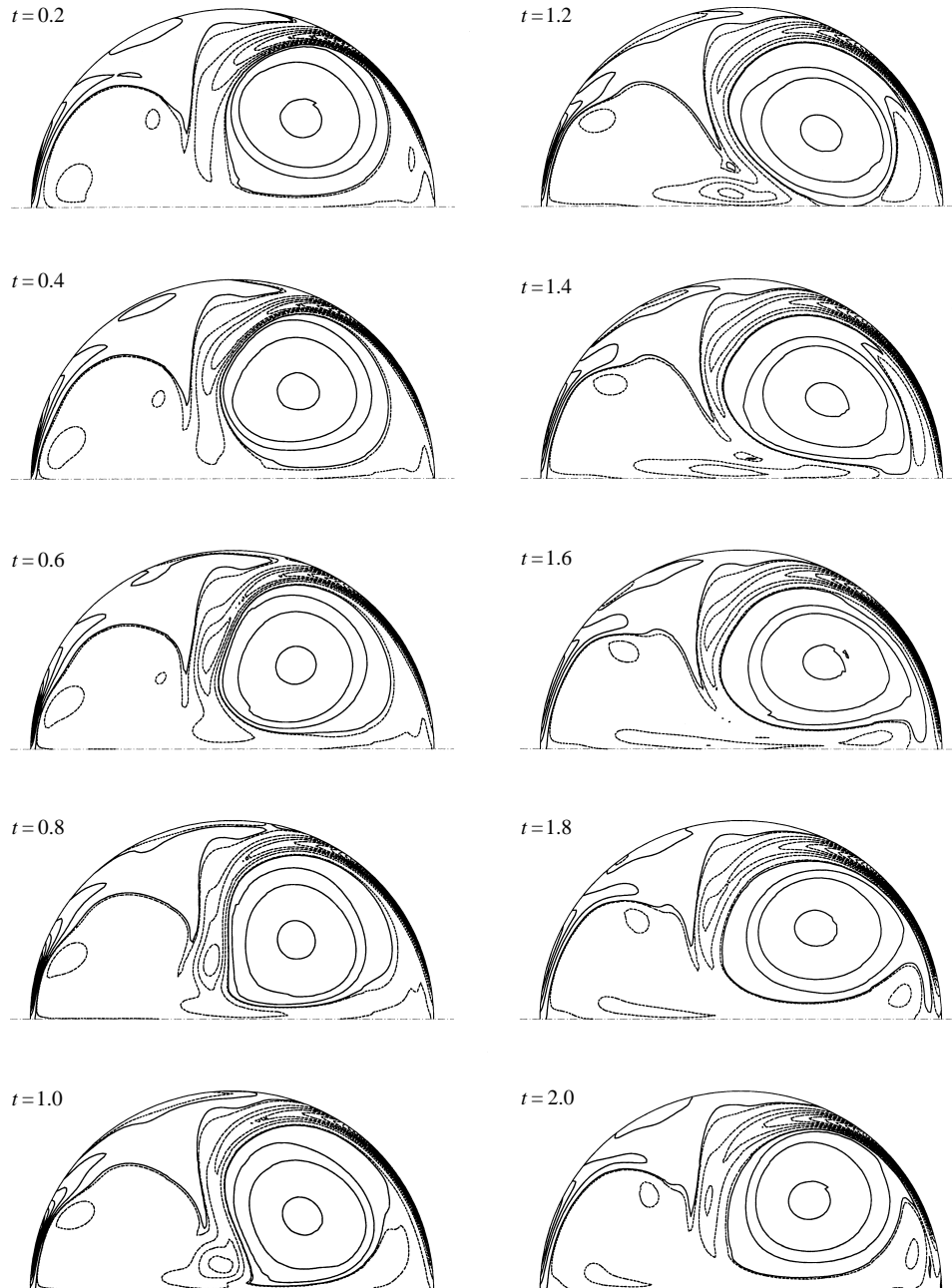
FIGURE 14. A sequence of instantaneous constant vorticity contour plots for one limit cycle with $\epsilon = 0.1$, $R_F = 13$.

whose magnitude is sufficient to sustain an energy flux equal to the boundary layer dissipation. It was to resolve these questions that we initiated numerical experiments for a simple model problem. Perhaps our single most important finding is that, at least for our model problem, no such steady, stable solutions exist. Rather, at a very modest Reynolds numbers, of around 10–20, the flow becomes unstable via a
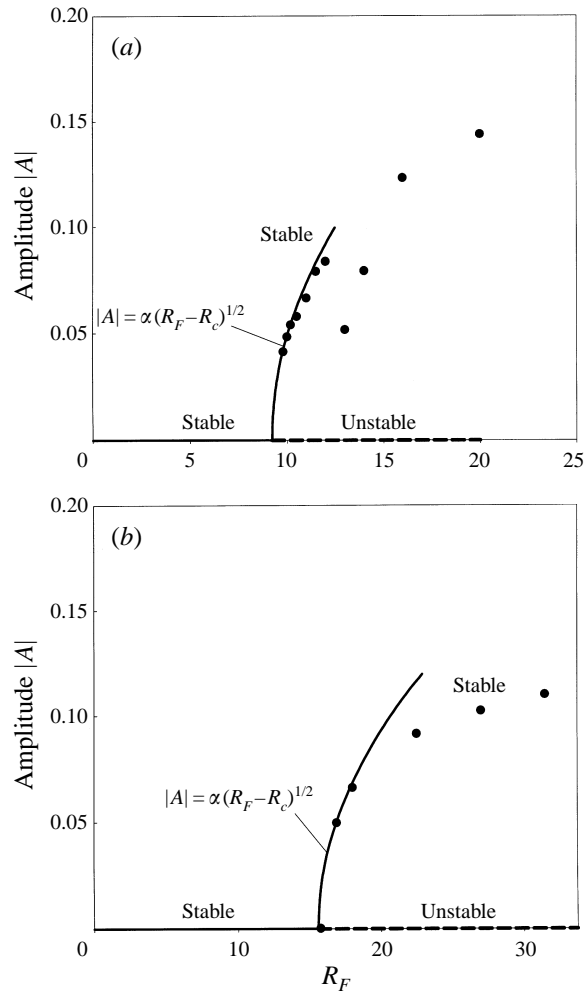
FIGURE 15. Bifurcation diagrams for the unsteady flow: (*a*) $\epsilon = 0.1$ (*b*) $\epsilon = 0.15$.

ϵ	$(R_F)_c$	$(Re)_c$
0.05	4.5–5.0	6.1–7.2
0.1	9.1	15.3
0.15	15.6	30.6
0.2	24–26	51–58

TABLE 2. Critical Reynolds numbers at four values of ϵ.

supercritical Hopf bifurcation. At this relatively low Reynolds number there is little or no hint of a high-Reynolds-number asymptotic structure in the flow. Specifically, there is little difference in the length scales of the forced and dissipative regions, so that our energy dilemma is not put to the test. Roughly, this transition to unsteady
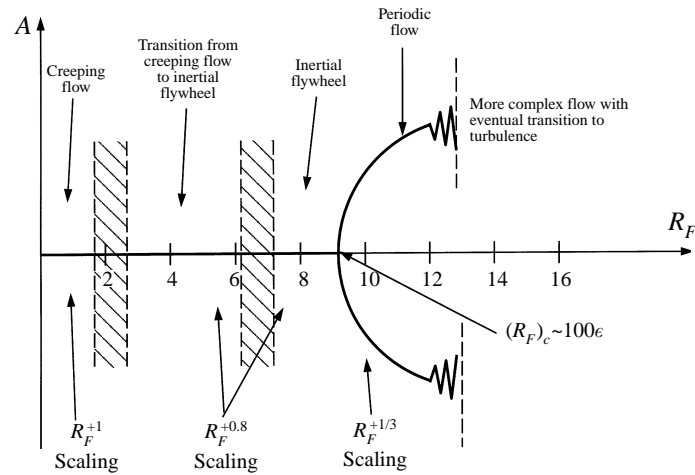
FIGURE 16. Our interpretation of the numerical experiments. (The exact divisions between the different regions depends on the value of ϵ.)

flow occurs at

$$\frac{u^* \delta_F}{\nu} \sim 100.$$

The initial instability is due to the formation of blobs of vorticity being shed from the separated shear layer. At higher Reynolds numbers the flow loses its periodicity and a more complex structure develops. Of course, several features of our model have limited the instabilities that might otherwise have developed. First, if we allowed a third dimension, then Taylor-like vortices are possible (see for example Davidson *et al.* 1995). Second, the symmetry boundary we impose eliminates the possibility of a symmetry-breaking instability. Which of the instabilities would occur first in practice we cannot say.

Our interpretation of our numerical results is illustrated in figure 16. Here, three different velocity scalings are identified: R_F^1 for creeping flows, $R_F^{0.8}$ for moderate (< 10) Reynolds numbers, and $R_F^{1/3}$ for periodic, unsteady flows.

REFERENCES

BATCHELOR, G. K. 1956 On steady laminar flows with closed streamlines at large Reynolds number. *J. Fluid Mech.* **1**, 177–398.

CLEVER, R. M. & BUSSE, F. H. 1981 Low-Prandtl-number convection in a layer heated from below. *J. Fluid Mech.* **102**, 61–74.

DAVIDSON, P. A. 1992 Swirling flow in an axisymmetric cavity of arbitrary profile, driven by a rotating magnetic field. *J. Fluid Mech.* **245**, 669–699.

DAVIDSON, P. A., SHORT, D. J. & KINNEAR, D. 1995 The role of Ekman pumping in confined MHD flows. *Eur. J. Mech.* B/*Fluids* **14**, 795–821.

DRAZIN, P. G. & REID, W. H. 1981 *Hydrodynamic Stability*. Cambridge University Press.

FAUTRELLE, Y. R. 1981 Analytical and numerical aspects of the electromagnetic stirring induced by alternating magnetic fields. *J. Fluid Mech.* **102**, 405–430.

MESTEL, A. J. 1984 On the flow in a channel induction furnace. *J. Fluid Mech.* **147**, 431–447.

MESTEL, A. J. 1989 An iterative method for high Reynolds number flows with closed streamlines. *J. Fluid Mech.* **200**, 1–18.

MOFFATT, H. K. 1978 Some problems in the magnetohydrodynamics of liquid metals. *Z. Angew. Math. Mech.* **58**, T65–T71.

PAIN, C. C. 1991 Finite element simulation of polyurethane foaming processes. PhD thesis, Exeter University.

SNEYD, A. D. 1979 Fluid flow induced by a rapidly alternating or rotating magnetic field. *J. Fluid Mech.* **92**, 35–51.